Open access • Posted Content • DOI:10.1101/2020.09.04.283358

Clustering analysis of single nucleotide polymorphism data reveals population structure of SARS-CoV-2 worldwide — Source link

Yawei Li, Qingyun Liu, Yuan Luo

Institutions: Northwestern University, Harvard University

Published on: 04 Sep 2020 - bioRxiv (Cold Spring Harbor Laboratory)

Topics: Hierarchical clustering, Cluster analysis and Population

Unsupervised clustering analysis reveals global population structure of SARS-CoV-2

Yawei Li[1], Qingyun Liu[2], Zexian Zeng[3], Yuan Luo[1*]

[1] Department of Preventive Medicine, Northwestern University, Feinberg School of Medicine, Chicago, IL 60611, USA

[2] Department of Immunology and Infectious Diseases, Harvard T. H. Chan School of Public Health, Boston, MA 02115, USA.

[3] Department of Data Science, Dana Farber Cancer Institute, Harvard T.H. Chan School of Public Health, Boston, MA 02215, USA

[*] Corresponding author:

Email: yuan.luo@northwestern.edu

Abstract

Identifying the population structure of the newly emerged coronavirus SARS-CoV-2 has significant potential to inform public health management and diagnosis. As SARS-CoV-2 sequencing data accrued, grouping them into clusters is important for organizing the landscape of the population structure of the virus. Since we have little prior information about the newly emerged coronavirus, we applied a state-of-the-art unsupervised deep learning clustering algorithm to group 16,873 SARS-CoV-2 strains, which automatically enables the identification of spatial structure for SARS-CoV-2. A total of six distinct genomic clusters were identified using mutation profiles as input features. The varied proportions of the six clusters within different continents revealed specific geographical distributions. Comprehensive analysis indicated that genetic factors and human migration played an important role in shaping the specific geographical distribution of population. This study provides a concrete framework for the use of clustering methods to study the global population structure of SARS-CoV-2. In addition, clustering methods can be used for future studies of variant population structures in specific regions of these fast-growing viruses.

Introduction

The COVID-19 pandemic was caused by severe acute respiratory syndrome coronavirus 2 (SARS-CoV-2) [1, 2], and has spread throughout the world. In an effort to understand the molecular characteristics of the virus, viral genomes have been abundantly sequenced and presented at the Global Initiative on Sharing All Influenza Data (GISAID). As an emerging virus, it is important to understand the genetic diversity, evolutionary trajectory and possible routes of transmission of SARS-CoV-2 from its natural reservoir to humans. Most studies have looked into the aspects of real-world SARS-CoV-2 evolution and strain diversification through phylogenetic trees [4, 5, 6]. Phylogenetic tree is a graph that shows the evolutionary relationships among various biological entities based on their genetic closeness [7, 8]. The distances from one entity to the other entities indicate the degree of relationships. However, as population genomic datasets grow in size, simply using pairwise genetic distances cannot present an explicit structure of the total population in phylogenetic analysis. Grouping similar entities into the same cluster and identifying the number of main subtypes (clusters) makes it easier to understand the main characteristics of the population. Traditionally, using the distance matrix and the bifurcations between branches of leaves on the phylogenetic tree, entities can be grouped into clusters. However, when the number of entities becomes large, it is not easy to directly and accurately partition the clades in the phylogenetic tree.

In order to identify a better way to effectively group entities, clustering methods emerge as more productive and robust solutions. The objective of clustering is automatically minimizing intra-cluster distances and maximizing inter-cluster distances [9]. Accurate clustering helps to better understand the inner relationships between data and inform downstream analysis. Clustering methods have been widely used as a good supplemental tool in phylogenetic analysis, including phylogenetic tree construction [10, 11, 12], ancestral relationship identification [13], evolutionary rate estimation [14, 15], gene evolutionary mechanisms research [16] and population structure analysis [17].

Herein, to identify the population structure of the newly emerged coronavirus SARS-CoV-2, we took inspiration from recent state-of-the-art deep embedding clustering method [18] to group a total of 16,873 strains. Compared with traditional methods, this deep learning clustering algorithm showed significant improvements in terms of both Silhouette score, sum of squared errors (SSE) and Bayesian information criterion (BIC) [19]. The clustering results showed that there were six major clusters of SARS-CoV-2. In particular, we found that the proportions of six clusters in each continent showed a specific geographical distribution. Our analysis revealed that the unique geographical distributions across the clusters are both influenced by intrinsic genetic factors and migration of humans. This study provides a perspective of the SARS-CoV-2 population structural analysis, helping to investigate the evolution and spread of the virus across the human populations worldwide.

Results

Genetic analysis indicates high diversity and rapidly proliferating of SARS-CoV-2

We obtained a total of 16,873 (98 from Africa, 1324 from Asia, 9527 from Europe, 4765 from North America, 1040 from

Oceania and 119 from South America) earliest SARS-CoV-2 whole-genome sequencing data from GISAID, aligned the sequences, and identified the genetic variants. A total of 7,970 substitutions were identified, including 4,908 non-synonymous mutations, 2,748 synonymous mutations and 314 intronic mutations. The average mutation count per genome was 6.99 (Figure S1). The frequency spectrum of substitutions illustrated that more than half (54.05%) of the mutations were singletons and 15.35% were doubletons. The proportion of the mutations below 0.01 was 99.28% (Figure S2). The high percentage of these low-frequency mutations suggested that SARS-CoV-2 occurred recently and displayed a rapidly proliferating pattern [20]. In addition, there were 8,706 unique strains across the 16,873 strains (Figure S3), and most unique strains (7,078) were singletons, yielding high diversity of the virus. In particular, Simpson's diversity index of the strains was 0.8222, indicating that two random strains would have a high probability of being genetically different. The frequency spectrum of substitutions and high Simpson's diversity index indicated high genetic diversity of SARS-CoV-2.

Clustering of SARS-CoV-2 reveals six major clusters

To clarify the main population structure of the virus, grouping these strains into clusters is necessary, as these clusters displayed the major types of the virus. However, the genetic analysis of SARS-CoV-2 showed that there were 8,706 unique strains across the 16,873 strains (Figure S3), it is not easy to directly and accurately partition the strains. For this reason, we applied clustering techniques to measure similarities between these strains and effectively group them.

Because SARS-CoV-2 exhibits a limited number of SNPs per virus strain and little ongoing horizontal gene exchange, making SNPs ideal clustering input features. We first used the aggregated SNP matrix to cluster samples using an unsupervised deep learning clustering algorithm [18] (see Methods). The unsupervised deep learning clustering algorithm requires one to pre-specify the number of clusters (*K*), but we have little prior knowledge about the number of subtypes formed by the heterogeneous SARS-CoV-2 genome. To determine the number of clusters, we plotted the curves of the SSE and BIC under different cluster numbers ranging from 2 to 20 (Figure S4). We used the elbow method and chose the elbow of the curve as the number of clusters [21]. This approach resulted in *K*=6 for both the SSE and BIC curves. To evaluate the performance of the algorithm, we also employed K-means clustering [22], hierarchical clustering and BIRCH clustering [23, 24] for comparison. The objective of clustering is minimizing intra-cluster distances and maximizing inter-cluster distances. To this end, we did five repetitions for each of the four clustering algorithms and selected the one that achieved the best performance (lowest average intra-cluster pairwise genetic distances). The average intra-cluster pairwise genetic distances in the deep learning clustering algorithm (4.892) was significantly lower than that in K-means (4.896, P-value < 0.001, Wilcoxon rank-sum test), hierarchical clustering (5.062, P-value < 0.001, Wilcoxon rank-sum test) and BIRCH (4.985, P-value < 0.001, Wilcoxon rank-sum test). We compared the Silhouette score (Figure 1A), SSE (Figure 1B) and BIC (Figure 1C) of the four algorithms. The deep learning clustering obtained the highest Silhouette score and BIC, and the lowest SSE, indicating that the clustering results of deep learning clustering are better than the other algorithms. In contrast, BIRCH performed the worst of the four algorithms. We aligned the partitions of the six clusters against the phylogenetic tree for the three best methods (Figure 1D). The clustering results indicated that the partitions from the three algorithms were similar. The differences between the hierarchical clustering results and the two other clustering results were mainly at the boundary of the clusters. Of the three methods, strains grouped by deep learning clustering and K-means were more compact in the phylogenetic tree than those by hierarchical clustering. For example, the strains in both deep learning clustering cluster D and K-means cluster D were split into two clusters using hierarchical clustering. However, such a split was not supported by the phylogenetic tree (Figure 1D).

In the meantime, we used complementary approaches to validate the deep learning clustering results. First, we compared the pairwise genetic distances between intra-cluster and inter-cluster. In all six clusters, the average number of intra-cluster genetic distances was significantly lower (P-value < 0.001, Wilcoxon rank-sum test, Figure 1E) than inter-cluster genetic distances. Next, we applied T-distributed Stochastic Neighbor Embedding (t-SNE) to visualize the deep learning clustering results. In the t-SNE plot, the strains were adequately isolated between clusters (Figure 1F).

The varied proportions of the clusters in different continents

Mapping the proportions of strains from each continent showed that the clusters differed in their geographical distributions (Figure 2, Table S1). Of the six clusters, cluster C spread globally. By contrast, cluster A and cluster F occurred at high frequencies in specific regions. 81.92% of the strains in cluster A and 85.73% of the strains in cluster F were from Europe. The geographical spread of each of the three remaining clusters was intermediate. Cluster E occurred at higher frequencies in North America and Europe, and lower frequencies in Asia and Oceania. Cluster D occurred at higher frequencies in North America, and lower frequencies in Asia, Europe and Oceania. The strains in cluster B were mainly in Asia and Europe and partially in North America and Oceania.

However, due to the sampling bias of the SARS-CoV-2, 85% of the strains were collected from Europe and North America (Table S1), making the proportion of the continents in each cluster not informative. Therefore, we evaluated the proportion of the clusters on each continent. In most continents, the distributions of the strains were concentrated in one or two clusters, including Asia (49% in cluster B), Africa (66% in cluster C), South America (78% in cluster C and F), North America (74% in cluster D and E) and Europe (64% in cluster C and F). Strikingly, Oceania was the only continent that was uniformly separated into the six clusters, indicating strains in Oceania were more diverse than in the other continents.

The different geographical distributions for the six clusters could be due to intrinsic genetic factors, extrinsic factors such as the migration of humans, or both. Hence, we next aimed to explore the genomic characteristics of these clusters, as well as the transmission and human migration of the virus across the globe.

The genetic variance analyses indicated high diversity between clusters

If the different geographical distributions for the six clusters were due to intrinsic genetic factors, there would be high genetic variance between the clusters. The average mutation counts for the six clusters were 6.38, 3.49, 6.57, 7.09, 7.89 and 8.96 (Figure S5), respectively. Considering the different collection dates (Figure 3A) of the strains, mutation rates as opposed to mutation counts were more effective for describing the genetic variations between clusters. We defined the date when the reference strain was collected as the index date. The average mutation rates for the six clusters were 25.55, 15.91, 25.44, 31.64, 30.99 and 34.12 substitutions per year, respectively. Specifically, the average mutation rate in cluster B was significantly lower (P-value < 0.001, Wilcoxon rank-sum test) than those in other clusters. In contrast, the average mutation rate in cluster F was significantly higher (P-value < 0.001, Wilcoxon rank-sum test) than those in other clusters. The Simpson's diversity indexes for the six clusters were 0.7616, 0.7608, 0.8398, 0.8466, 0.8082 and 0.8502, respectively. Both the average mutation rate and Simpson's index were highest in cluster F, suggesting that the diversity of cluster F was higher than the other clusters. The nucleotide diversity per site for the six clusters was 0.0196%, 0.0222%, 0.0171%, 0.0256%, 0.0131% and 0.0132%. The high mutation rates but low nucleotide diversity in cluster E and cluster F suggests that these two clusters may have more fixed mutations than the other clusters. The nucleotide diversity of each gene across all clusters is displayed in Figure 3B-G. Except for some short genes that are unlikely to be informative, the diversity of most genes was close to the diversity of their genome-wide variants. Our analysis showed that intra-cluster genetic diversity differed between clusters, suggesting that selective pressures were different between clusters. These different selective pressures will affect the geographical distribution of each cluster.

Explore mutations that shaped the geographical distribution of population structure.

The high genetic diversity between clusters indicated that the frequencies of the mutations across clusters were very different. In order to explore whether there are mutations that affect the genetic structure within the clusters, we applied ANOVA to identify the statistically significant mutations that were strongly associated with clusters. Across the 7,970 substitutions, 26.27% (2,094 substitutions) of them achieved P-values <0.05 (Figure S6). We found that some of these mutations were fixed in one or several clusters. Cluster C, cluster E and cluster F shared four common fixed substitutions: A23403G, C241T, C3037T and C14408T. Cluster E had two additional fixed substitutions: C1059T and G25563T, and cluster F had three additional substitutions from position 28,881 to position 28,883. For the remaining three clusters, there were two fixed substitutions (C8782T, T28144C) and three fixed substitutions (G11083T, G14805T and G26144T) in cluster A. It is noteworthy that the fixed mutation numbers in cluster E (six) and cluster F (seven) were higher than in any of the other clusters, which was consistent with our conclusion of the high mutation rates but low nucleotide diversity in cluster E and cluster F.

We selected the 2% (42/2094) substitutions that achieved the lowest P-values (Table 1) and analyzed their distributions in the clusters. Of the 42 substitutions, there were 26 nonsynonymous mutations (mutation G28882A was in a trinucleotide mutation from position 28881 to 28883 that spans two codons and results in an RG (arginine-glycine) to KR (lysine-arginine) amino acid change). We focused on these nonsynonymous mutations as these mutations may be under selection that affect the population structure [25]. Some of these substitutions were reported to impact the evolution of SARS-CoV-2 [26, 27]. For example, mutation A23403G (D614G, Asparticacid to Glycine) in the *spike* protein domains was reported to show significant variation in cytopathic effects and viral load, and substantially change the pathogenicity of SARS-CoV-2 [28]. This mutation was accompanied by a mutation (T14408C) that results in an RNA-dependent RNA polymerase (RdRp) amino acid change [29]. In addition, Tang et al [30] used mutation T28144C to define “L” type (defined as “L” type because T28,144 is in the codon of Leucine) and “S” type (defined as “S” type because C28,144 is in the codon of Serine) of SARS-CoV-2. They found that the “L” type was more transmissible and aggressive than the “S” type.

Previous studies have reported that recombination is common in coronavirus [4, 31, 32]. Given that recombinations in SARS-CoV-2 may perturb the clustering, we used Haploview [33] to analyze the linkage disequilibrium (LD) by calculating standardized disequilibrium coefficients (D’) and squared allele-frequency correlations (r^2) of the 42 substitutions. D′ is affected solely by recombination and not by differences in allele frequencies between sites, and r^2 is also affected by differences in allele frequencies at the two sites. In the heatmap of D’ and r^2 (Figure S7), no obvious LD blocks were discovered, indicating that our clustering of SARS-CoV-2 strains using substitutions was not distorted by recombination.

Selection usually affects the distribution of the mutations in the population. Purifying selection tends to remove amino acid-altering mutations, while positive selection tends to increase the frequency of the mutations. Considering the rapidly proliferating pattern of SARS-CoV-2 that strengthened the power of drift relative to the power of purifying selection [34, 35, 36], we mainly focused on the positive selective sites. We applied HyPhy [37] to infer the probabilities of the extracted 26 nonsynonymous mutations that were under positive selection. There are nine mutations (asterisks in Table 1) with a positive probability >0.95. In particular, mutations G2891A, G11083T, C14408T, C17747T and A23403G (D614G) were reported as recurrent mutations [26, 38]. The recurrence of these mutations agrees with the assumption that they may confer selective advantages in the population. These possible positively selected mutations may result in greater diversity among clusters with different population structures of SARS-CoV-2 across geographical regions.

The global spread of SARS-CoV-2

Regardless of the genetic factors, the travel of humans could also lead to unique geographical distributions in today's highly globalized world. By analyzing the frequencies of the extracted 42 mutations in each cluster (Figure 4A) and their collected daily counts (Figure 4B), we can trace the dynamics of substitutions in the SARS-CoV-2 genome. The four genetically linked mutations, A23403G (D614G), C241T, C3037T and C14408T that were fixed across three clusters (C, E and F) had become the highest frequency mutations in the world, with a high frequency on all continents in our downloaded sequences, including South America (87%), Africa (86%), Europe (75%), North America (65%), Oceania (55%) and Asia (32%). The earliest time when sequences carrying these mutations was collected was in late January 2020. About a month later, these mutations were discovered worldwide. Though the mutation A23403G (D614G) has been reported and estimated to be a positive selective mutation, it is almost impossible to spread to the world without human migration in such a short time. Besides these high frequency mutations, some lower frequency mutations also provided some evidence of human migration. We explored the geographical distributions of mutations with global frequencies <0.05 in Table 1. Though most of these low frequency mutations were mainly collected within a single continent, we still find two mutations, T28688C and G1397A, were discovered in Asia, Europe and Oceania with high proportion. In addition, the spatial geographical distributions of some substitutions also provide the evidence that human migration may have influenced the spread of the virus. For example, on the west coast of the USA, most strains accumulated the mutations C8782T and T28144C (cluster D), and these mutations were also found in high frequencies in east Asia. In contrast, on the east coast of the USA, most strains accumulated the mutations A23403G, C241T, C3037T, C14408T, C1059T and G25563T (cluster E), and the similar strains were mainly discovered in Europe (Figure S8).

Discussion

Understanding the population structure of SARS-CoV-2 is important in evaluating future risks of novel infections. To precisely analyze their population structure, we used clustering methods in phylogenetic analysis to group a total of 16,873 publicly available SARS-CoV-2 strains. To improve the accuracy, we use a state-of-the-art deep learning clustering algorithm, which has been demonstrated to exhibit better performance than three traditional clustering algorithms: K-means clustering, hierarchical clustering and BIRCH.

Our clustering results indicated six major clusters of SARS-CoV-2. The mutation profile characterizing clusters of the viral sequences displayed specific geographical distributions. Most continents were mainly concentrated in one or two clusters, but we also found that in Oceania, the strains were uniformly separated across the six clusters. To evaluate whether the geographical distributions for the clusters were due to genetic factors or travel of humans. The varied intra-cluster genetic diversity across the clusters suggested different selective pressures between clusters, which would affect the geographical distributions across the clusters. By analyzing the statistically significant mutations that were strongly associated with the clusters we identified that some mutations might be under positive selection, indicating different geographical distributions between the clusters were partially affected by these mutations. In addition, the dynamics and the spatial geographical distributions of some substitutions suggested that human migration may also have affected the different geographical distributions. In general, our findings indicate that the geographical distributions for the clusters are the result of both genetic factors and migration of humans.

It is noteworthy that our study is limited due to the sampling bias of SARS-CoV-2, with more than 60% of the strains being from the United Kingdom and the USA. In contrast, the overall proportion of strains from Africa and South America is less than 2% (Table S1). Sampling biases can lead to biased parameter estimation and affect the clustering results we observed. For example, the frequency of mutation C15324T reached 41.84% in Africa, but was only 2.21% outside Africa. The frequency of mutation T29148C reached 15.13% in South America, but was only 0.12% outside South America. Another mutation T27299C with frequency 10.92% in South America was only found with frequency 0.08% in other regions. In fact, all three mutations were mostly grouped in single clusters, indicating these mutations were highly concentrated. However, due to the small proportion of the strains from these two continents, these mutations were unable to affect the clustering of samples. To address this issue, more strains were needed to be collected from these continents. In addition, we found that in cluster B, there were no fixed mutations. We calculated the pairwise dependency scores (see Methods) of all the mutations with frequencies >0.05 in cluster B and discovered five main subclusters (Figure S9). Other than the mutation G11083T that was discovered in two subclusters, there were no common mutations between either of the five clusters. As shown in Figure 3A, these strains were grouped in one cluster mainly because these strains had smaller mutation counts than strains in other clusters. The genetic distance between two strains was still small, though they shared no common mutations. To address this issue, another clustering can be used for more further analyses.

Despite the limited number of SARS-CoV-2 genome sequences, our analysis of population genetics is formative. Our discovery of high genetic diversity in SARS-CoV-2 is consistent with an earlier study [39]. The topology and the divergence of the clusters in the phylogenetic tree illustrate a relatively recent common ancestor, similar to the fact that the emergence and the spread of the virus was highly concentrated in a short time [2, 40, 41, 42]. Our work, as well as previous studies [43, 44] that use clustering techniques to study the population structure of the SARS-CoV-2 virus, has proved to be a valuable supplemental tool in phylogenetic analyses. In addition, clustering ideas can be used for further study of variant population structures in specific regions of these fast-growing viruses.

Methods

SARS-CoV-2 sample collection

A set of African, Asian, European, North American, Oceanian and South American SARS-CoV-2 strains marked as “high coverage" were downloaded from GISAID. The "high coverage" was defined as strains with <1% Ns and <0.05% unique amino acid mutations (not seen in other sequences in databases) and no insertion/deletion unless verified by the submitter. In addition, all strains with a non-human host and all assemblies of total genome length less than 29,000 bps were removed from our analysis. Ultimately, our dataset consisted of 16,873 strains.

Mutation calls and phylogenetic reconstruction

All downloaded genomes were mapped to the reference genome of SARS-CoV-2 (GenBank Accession Number: NC_045512.2) following Nextstrain pipeline [45]. Multiple sequence alignments and pairwise alignments were constructed using CLUSTALW 2.1 [46]. Considering many putatively artefactual mutations and the gaps in sequences are located at the beginning and end of the alignment, we masked the first 130 bps and last 50 bps in mutation calling following Nextstrain pipeline. We used substitutions as features to reconstruct the phylogenetic tree using FastTree 2 [47]. The phylogeny is rooted following Nextstrain pipeline using FigTree v1.4.4. The phylogenetic trees were visualized using the online tool Interactive Tree Of Life (iTOL v5) [48].

Region analysis and data visualization

For each country with SARS-CoV-2 data available, clustering proportions were calculated and plotted on the world map using the tool Tableau Desktop 2020.2. Other Figures and statistical analyses were generated by the ggplot2 library in R 3.6.1, the seaborn package in Python 3.7.6 and GraphPad Prism 8.0.2.

Data clustering

Herein, we employed a deep learning unsupervised clustering algorithm to iteratively cluster the SARS-CoV-2 strains [18]. Each identified cluster was considered to be a subtype of SARS-CoV-2. We first used K-means clustering to initialize centroids for the clusters. To determine the number of clusters, we plotted the curves of the sum of squared errors (SSE) and Bayesian information criterion (BIC) [19] under different cluster numbers ranging from 2 to 20.

To update the cluster assignments, we implemented the Student's t-distribution as a kernel to measure the distance from a strain (h_i) to a cluster centroid (u_j):

$$q_{ij} = \frac{(1+\left\|h_i - u_j\right\|^2/\alpha)^{-\frac{\alpha+1}{2}}}{\sum_{j'=1}^{K}(1+\left\|h_i - u_{j'}\right\|^2/\alpha)^{-\frac{\alpha+1}{2}}}$$

where the distance q_{ij} can be interpreted as the probability of assigning strain i to cluster j. The α is the degree of freedom of the Student's t-distribution, and we let $\alpha = 1$ in this study. Next, we defined an auxiliary target distribution P by raising each q_{ij} to the second power which upweights strains assigned with high confidence:

$$p_{ij} = \frac{q_{ij}^2/\sum_{i=1}^{N} q_{ij}}{\sum_{j'=1}^{K}(q_{ij'}^2/\sum_{i=1}^{N} q_{ij'})}$$

where the denominator is to normalize the loss contribution of each centroid to prevent large clusters from distorting the feature space. Finally, we defined the objective function using a Kullback-Leibler (KL) divergence loss:

$$\mathrm{L} = \mathrm{KL}(\mathrm{P}||\mathrm{Q}) = \sum_{i=1}^{N}\sum_{j=1}^{K} p_{ij} log\frac{p_{ij}}{q_{ij}}$$

The parameters and cluster centroids were jointly optimized by minimizing L using Stochastic Gradient Descent (SGD) with momentum.

Besides the deep learning clustering algorithm, we also employed K-means clustering, hierarchical clustering and BIRCH (Balanced Iterative Reducing and Clustering using Hierarchies) for SARS-CoV-2 strain clustering. The three models were implemented using the Python package sklearn with the KMeans function, AgglomerativeClustering function and Birch function, respectively.

Simpson's diversity index

Simpson's Diversity Index (*D*) is a measure of diversity that considers the number of entities as well as their abundance. The index measures the probability that two randomly selected individuals are the same. The formula to calculate the value of the index is:

$$\mathrm{D} = 1 - \frac{\sum_{all\ traits} n(n-1)}{N(N-1)}$$

where n is the number of individuals displaying one trait and N is the total number of all individuals. The value of D ranges between 0 and 1. With this index, 1 represents infinite diversity and 0 denotes no diversity.

Inferring positive/purifying selection of individual sites

To test which position was under selective pressure, we used a set of programs available in HyPhy to calculate nonsynonymous (dN) and synonymous (dS) substitution rates on a per-site basis to infer pervasive selection. Fast Unconstrained Bayesian AppRoximation (FUBAR) was applied to detect overall sites under positive selection. The positively selected sites were identified using a probability larger than 0.95 using the FUBAR method.

Pairwise mutation dependency score

Pairwise mutation dependency scores can measure the order in which genetic mutations are acquired within a cluster. For two selected mutations X and Y, the score S(X|Y) represents the proportion of strains that accumulated both X among the strains that accumulated mutation Y. S(X|Y) and S(Y|X) can be calculated using the following functions:

$$\mathrm{S(X|Y)} = \frac{\sum_{all\ samples} S_X = 1 \ \&\ S_Y = 1}{\sum_{all\ samples} S_Y = 1}$$

$$\mathrm{S(Y|X)} = \frac{\sum_{all\ samples} S_X = 1 \ \&\ S_Y = 1}{\sum_{all\ samples} S_X = 1}$$

where $S_X = 1$ denotes that the sequence has a mutation X. Pairwise mutation dependency score displays the correlation and the timescale relationship of the two mutations. The value of S(X|Y) and S(Y|X) ranges between 0 and 1. With this index, S(X|Y) = 1 with S(Y|X) < 1 represents that mutation Y occurs after mutation X. In contrast, S(X|Y) = 1 with S(Y|X) = 1 represents that the two mutations occur simultaneously and are genetically linked. Statistical analyses and data presentations were generated using Python 3.7.6.

Data Availability

The publicly available SARS-CoV-2 datasets in this study are available at GISAID (https://www.gisaid.org). The reference SARS-CoV-2 is available at the NCBI GenBank (GenBank Accession Number: NC_045512.2, https://www.ncbi.nlm.nih.gov/nuccore/NC_045512.2).

References

1. Coronaviridae Study Group of the International Committee on Taxonomy of V. The species Severe acute respiratory syndrome-related coronavirus: classifying 2019-nCoV and naming it SARS-CoV-2. *Nat Microbiol* **5**, 536-544 (2020).

2. Zhu N*, et al.* A Novel Coronavirus from Patients with Pneumonia in China, 2019. *N Engl J Med* **382**, 727-733 (2020).

3. Li R*, et al.* Substantial undocumented infection facilitates the rapid dissemination of novel coronavirus (SARS-CoV-2). *Science* **368**, 489-493 (2020).

4. Rehman SU, Shafique L, Ihsan A, Liu Q. Evolutionary Trajectory for the Emergence of Novel Coronavirus SARS-CoV-2. *Pathogens* **9**, (2020).

5. Forster P, Forster L, Renfrew C, Forster M. Phylogenetic network analysis of SARS-CoV-2 genomes. *Proc Natl Acad Sci U S A* **117**, 9241-9243 (2020).

6. Koyama T, Platt D, Parida L. *Variant analysis of COVID-19 genomes* (2020).

7. Mahapatro G, Mishra D, Shaw K, Mishra S, Jena T. Phylogenetic Tree Construction for DNA Sequences using Clustering Methods. *Procedia Engineer* **38**, 1362-1366 (2012).

8. Sharma A, Jaloree S, Thakur R. Review of Clustering Methods: Toward Phylogenetic Tree Constructions. 475-480 (2018).

9. Gonzalez TF. Clustering to minimize the maximum intercluster distance. *Theoretical Computer Science* **38**, 293-306 (1985).

10. Wang J, Soininen J, He J, Shen J. Phylogenetic clustering increases with elevation for microbes. *Environ Microbiol Rep* **4**, 217-226 (2012).

11. Ning J, Beiko RG. Phylogenetic approaches to microbial community classification. *Microbiome* **3**, 47 (2015).

12. Fioravanti D*, et al.* Phylogenetic convolutional neural networks in metagenomics. *BMC Bioinformatics* **19**, 49 (2018).

13. Qin L, Chen YX, Pan Y, Chen L. A novel approach to phylogenetic tree construction using stochastic optimization and clustering. *Bmc Bioinformatics* **7**, (2006).

14. Felsenstein J, Churchill GA. A hidden Markov Model approach to variation among sites in rate of evolution. *Mol Biol Evol* **13**, 93-104 (1996).

15. Siepel A*, et al.* Evolutionarily conserved elements in vertebrate, insect, worm, and yeast genomes. *Genome Res* **15**, 1034-1050 (2005).

16. Medema MH, Cimermancic P, Sali A, Takano E, Fischbach MA. A systematic computational analysis of biosynthetic gene cluster evolution: lessons for engineering biosynthesis. *PLoS Comput Biol* **10**, e1004016 (2014).

17. Han E*, et al.* Clustering of 770,000 genomes reveals post-colonial population structure of North America. *Nat Commun* **8**, 14238 (2017).

18. Xie J, Girshick R, Farhadi A. Unsupervised deep embedding for clustering analysis. In: *Proceedings of the 33rd International Conference on International Conference on Machine Learning - Volume 48*). JMLR.org (2016).

19. Schwarz G. Estimating the Dimension of a Model. *Ann Statist* **6**, 461-464 (1978).

20. Yu WB, Tang GD, Zhang L, Corlett RT. Decoding the evolution and transmissions of the novel pneumonia coronavirus (SARS-CoV-2 / HCoV-19) using whole genomic data. *Zool Res* **41**, 247-257 (2020).

21. Thorndike RL. Who Belongs in the Family? *Psychometrika* **18**, 267-276 (1953).

22. MacQueen J. Some methods for classification and analysis of multivariate observations. In: *Proceedings of the Fifth Berkeley Symposium on Mathematical Statistics and Probability, Volume 1: Statistics*). University of California Press (1967).

23. Zhang T, Ramakrishnan R, Livny M. BIRCH: an efficient data clustering method for very large databases. In:

Proceedings of the 1996 ACM SIGMOD international conference on Management of data). Association for Computing Machinery (1996).

24. Zhang T, Ramakrishnan R, Livny M. BIRCH: A New Data Clustering Algorithm and Its Applications. *Data Mining and Knowledge Discovery* **1**, 141-182 (1997).

25. Hartl DL, Clark AG. *Principles of population genetics*, 4th edn. Sinauer Associates (2007).

26. van Dorp L*, et al.* Emergence of genomic diversity and recurrent mutations in SARS-CoV-2. *Infect Genet Evol* **83**, 104351 (2020).

27. Yin C. Genotyping coronavirus SARS-CoV-2: methods and implications. *Genomics*, (2020).

28. Yao H*, et al.* Patient-derived mutations impact pathogenicity of SARS-CoV-2. *medRxiv*, 2020.2004.2014.20060160 (2020).

29. Korber B*, et al.* Tracking Changes in SARS-CoV-2 Spike: Evidence that D614G Increases Infectivity of the COVID-19 Virus. *Cell* **182**, 812-+ (2020).

30. Tang X*, et al.* On the origin and continuing evolution of SARS-CoV-2. *National Science Review*, (2020).

31. Graham RL, Baric RS. Recombination, reservoirs, and the modular spike: mechanisms of coronavirus cross-species transmission. *J Virol* **84**, 3134-3146 (2010).

32. Rouchka E, Chariker J, Chung D. Phylogenetic and Variant Analysis of 1,040 SARS-CoV-2 Genomes. (2020).

33. Barrett JC, Fry B, Maller J, Daly MJ. Haploview: analysis and visualization of LD and haplotype maps. *Bioinformatics* **21**, 263-265 (2005).

34. Nowak MA, Michor F, Iwasa Y. The linear process of somatic evolution. *Proc Natl Acad Sci U S A* **100**, 14966-14969 (2003).

35. Wu CI, Wang HY, Ling S, Lu X. The Ecology and Evolution of Cancer: The Ultra-Microevolutionary Process. *Annu Rev Genet* **50**, 347-369 (2016).

36. Chen Y, Tong D, Wu CI. A New Formulation of Random Genetic Drift and Its Application to the Evolution of Cell Populations. *Mol Biol Evol* **34**, 2057-2064 (2017).

37. Pond SLK*, et al.* HyPhy 2.5-A Customizable Platform for Evolutionary Hypothesis Testing Using Phylogenies. *Mol Biol Evol* **37**, 295-299 (2020).

38. Pachetti M*, et al.* Emerging SARS-CoV-2 mutation hot spots include a novel RNA-dependent-RNA polymerase variant. *J Transl Med* **18**, 179 (2020).

39. Li X*, et al.* Transmission dynamics and evolutionary history of 2019-nCoV. *J Med Virol* **92**, 501-511 (2020).

40. Chan JFW*, et al.* A familial cluster of pneumonia associated with the 2019 novel coronavirus indicating person-to-person transmission: a study of a family cluster. *Lancet* **395**, 514-523 (2020).

41. Sun J*, et al.* COVID-19: Epidemiology, Evolution, and Cross-Disciplinary Perspectives. *Trends Mol Med* **26**, 483-495 (2020).

42. Zhou P*, et al.* A pneumonia outbreak associated with a new coronavirus of probable bat origin. *Nature* **579**, 270-273 (2020).

43. Mishra A*, et al.* Mutation landscape of SARS-CoV-2 reveals three mutually exclusive clusters of leading and trailing single nucleotide substitutions. *bioRxiv*, 2020.2005.2007.082768 (2020).

44. Seemann T*, et al.* Tracking the COVID-19 pandemic in Australia using genomics. *Nature Communications* **11**, 4376 (2020).

45. Hadfield J*, et al.* Nextstrain: real-time tracking of pathogen evolution. *Bioinformatics* **34**, 4121-4123 (2018).

46. Larkin MA*, et al.* Clustal W and Clustal X version 2.0. *Bioinformatics* **23**, 2947-2948 (2007).

47. Price MN, Dehal PS, Arkin AP. FastTree 2--approximately maximum-likelihood trees for large alignments. *PLoS One* **5**, e9490 (2010).

48. Letunic I, Bork P. Interactive Tree Of Life (iTOL): an online tool for phylogenetic tree display and annotation. *Bioinformatics* **23**, 127-128 (2007).

Competing Interests

The authors declare no competing interests.

Authors' contributions

Y.Luo and Y.Li designed the research; Y.Li and Q.L. analyzed data; Y.Luo, Y.Li and Q.L. contributed to the theory; and Y.Luo and Y.Li drafted the manuscript. All authors have read, edited and approved the final manuscript.

Table 1. The information of the 42 mutations using ANOVA.

Mutation	Substitution	Amino Acid Substitution	Type	GENE	Frequency	Cluster					
						A	B	C	D	E	F
C241T	C > T	Intron	Intron	Intron	66.37%	10	10	4238	2	3548	3391
T490A	T > A	D > E	N	ORF1ab	1.04%	0	0	1	174	0	0
T514C	T > C	H > H	S	ORF1ab	0.97%	0	162	1	0	0	0
C1059T*	C > T	T > I	N	ORF1ab	21.69%	1	8	2	0	3645	3
G1397A	G > A	V > I	N	ORF1ab	1.12%	0	186	0	0	1	2
G1440A	G > A	G > D	N	ORF1ab	1.92%	0	324	0	0	0	0
A2480G	A > G	I > V	N	ORF1ab	3.60%	608	0	0	0	0	0
C2558T	C > T	P > S	N	ORF1ab	3.83%	646	1	0	0	0	0
G2891A*	G > A	A > T	N	ORF1ab	1.77%	0	298	0	0	0	0
C3037T	C > T	F > F	S	ORF1ab	67.26%	2	7	4277	3	3611	3448
C3177T	C > T	P > L	N	ORF1ab	1.05%	0	0	1	171	6	0
C6312A	C > A	T > K	N	ORF1ab	1.14%	0	189	1	0	0	3
C8782T	C > T	S > S	S	ORF1ab	11.42%	1	21	5	1898	1	1
T9477A	T > A	F > Y	N	ORF1ab	1.17%	0	3	0	195	0	0
G11083T*	G > T	L > F	N	ORF1ab	11.81%	1342	485	52	21	54	39
C14408T*	C > T	P > L	N	ORF1ab	67.47%	1	8	4301	2	3636	3436
C14805T	C > T	Y > Y	S	ORF1ab	9.39%	1352	8	1	195	0	28
T17247C	T > C	R > R	S	ORF1ab	3.00%	500	5	1	0	0	0
C17747T*	C > T	P > L	N	ORF1ab	6.92%	1	0	0	1165	1	0
A17858G	A > G	Y > C	N	ORF1ab	7.05%	1	1	0	1187	0	0
C18060T	C > T	L > L	S	ORF1ab	7.16%	0	3	2	1202	1	0
T18736C	T > C	F > L	N	ORF1ab	1.01%	0	0	1	169	0	0
C18877T	C > T	L > L	S	ORF1ab	2.67%	2	2	440	4	0	2
A20268G	A > G	L > L	S	ORF1ab	4.61%	0	1	773	3	0	1
A23403G*	A > G	D > G	N	S	67.65%	4	4	4316	6	3634	3451
C23731T	C > T	T > T	S	S	1.68%	0	0	0	0	1	282
C23929T	C > T	Y > Y	S	S	1.13%	0	186	1	0	1	2
C24034T	C > T	N > N	S	S	1.16%	0	2	1	187	4	1
G25563T*	G > T	Q > H	N	ORF3a	26.44%	1	3	829	2	3625	2
G25979T	G > T	G > V	N	ORF3a	1.16%	0	2	1	193	0	0
G26144T*	G > T	G > V	N	ORF3a	8.61%	1387	62	0	1	1	1
T26729C	T > C	A > A	S	M	1.07%	0	1	1	179	0	0
C27046T	C > T	T > M	N	M	2.13%	0	1	5	0	0	353
G28077C	G > C	V > L	N	ORF8	1.13%	0	1	1	188	0	0
T28144C*	T > C	L > S	N	ORF8	11.36%	0	10	1	1903	2	0
C28657T	C > T	D > D	S	N	1.21%	0	3	3	196	1	2
T28688C	T > C	L > L	S	N	1.07%	0	178	1	0	1	0
C28863T	C > T	S > L	N	N	1.19%	1	2	2	193	2	0
G28881A	G > A	R > K	N	N	20.54%	4	3	3	1	1	3453
G28882A	G > A	R > K[1]	N	N	20.49%	1	2	0	0	0	3454
G28883C	G > C	G > R	N	N	20.49%	1	2	1	0	0	3453
A29700G	A > G	Intron	Intron	Intron	1.04%	0	0	4	167	4	1

[1] G28881A and G28882A occur within the same codon. Amino acid annotation (R > K) is based on the co-occurrence of these mutations.

* Under positive selection inferred by HyPhy.

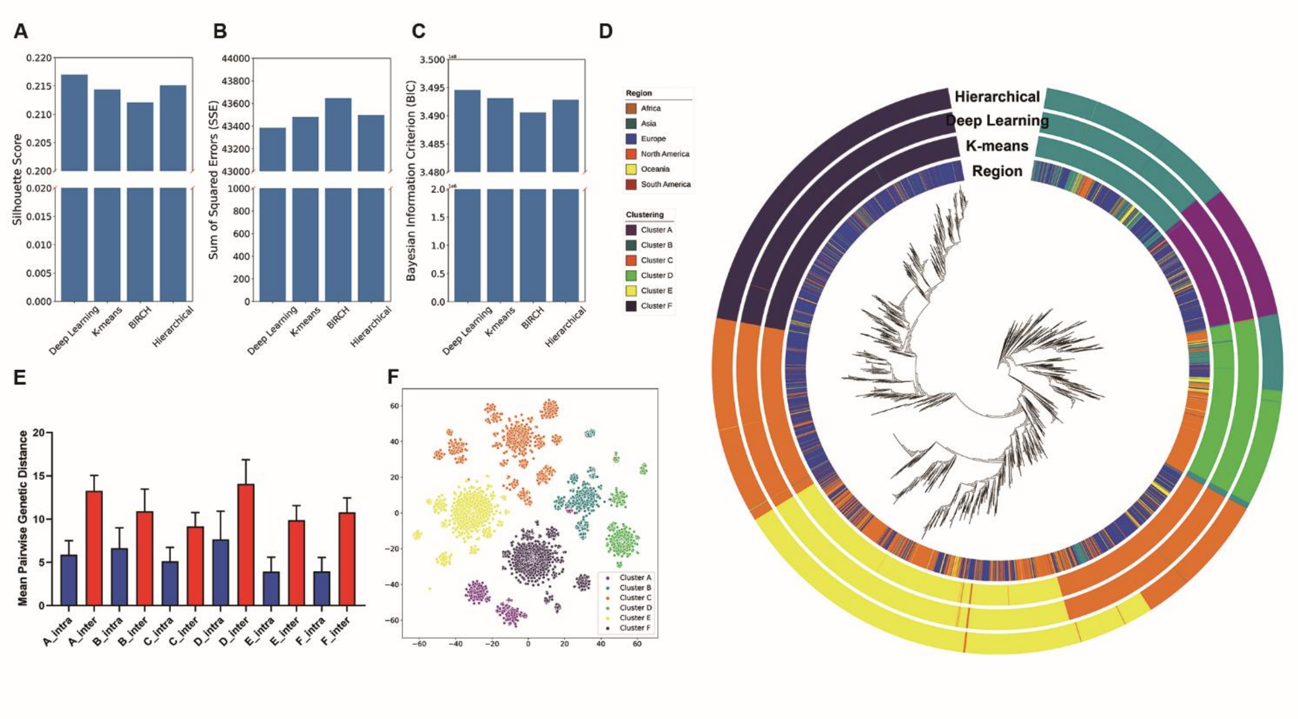

Figure 1. Clustering of SARS-CoV-2. (**A, B** and **C**) The Silhouette score (A), Sum of Squared Errors (SSE; B) and Bayesian Information Criterion (BIC; C) for the four selected algorithms (X axis). (**D**) Phylogenetic tree of 16,873 SARS-CoV-2 strains. Four colored panels outside the phylogenetic tree are used to identify auxiliary information for each virus strain. The inner panel represents the distribution of the continents. The outer three panels represent the partitions of the six clusters across the three best performance clustering algorithms (deep learning, K-means and Hierarchical) in the tree. (**E**) Mean pairwise genetic distances for intra-clustered and inter-clustered genetic distances. The blue bars represent mean pairwise genetic distances between pairs of isolates within the clusters, and the red bars represent mean pairwise genetic distances between pairs of isolates outside the clusters. The error bar represents the standard deviation. The mean distance between pairs of strains for intra-clusters was significantly lower (P-value < 0.001, Wilcoxon rank-sum test) than that of inter-clusters. (**F**) The t-SNE plot of the deep learning clustering results. Each dot represents one strain and each color represents the corresponding cluster.

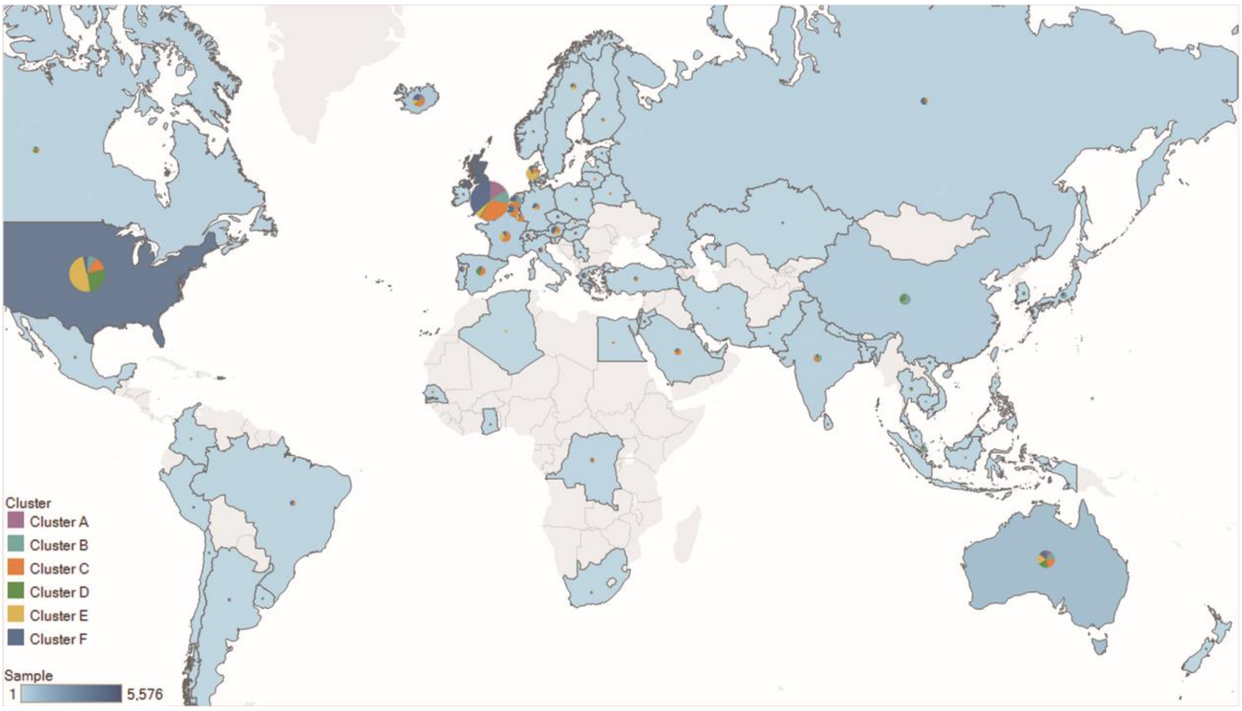

Figure 2. Geographic distributions of the six clusters. Pie charts display the proportions of six clusters among all SARS-CoV-2 strains in each country. Circle sizes and the color scales correspond to the number of strains analyzed per country.

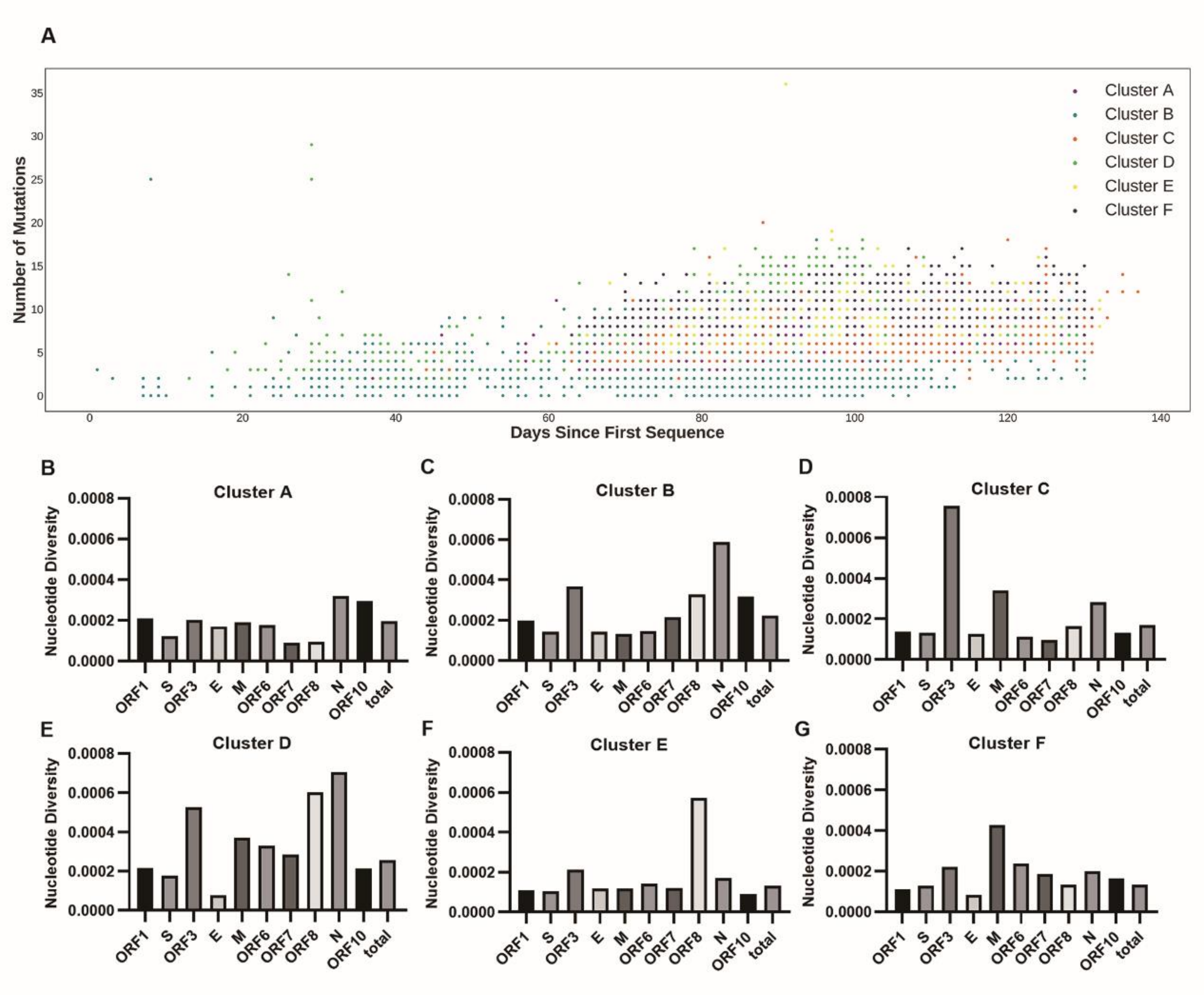

Figure 3. The genetic diversity between clusters. (**A**) The mutation counts over days of 16,873 SARS-CoV-2 strains. The X axis represents the days from the corresponding collection date of strains to 24 December 2019 when the earliest strain (EPI_ISL_402123) was collected. The Y axis represents the number of mutations of each collected strain. A mutation is defined by a nucleotide change from the original nucleotide in the reference genome to the alternative nucleotide in the studied viral genome. (**B-G**) The nucleotide diversity (π) per site for each gene and genome-wide across six clusters.

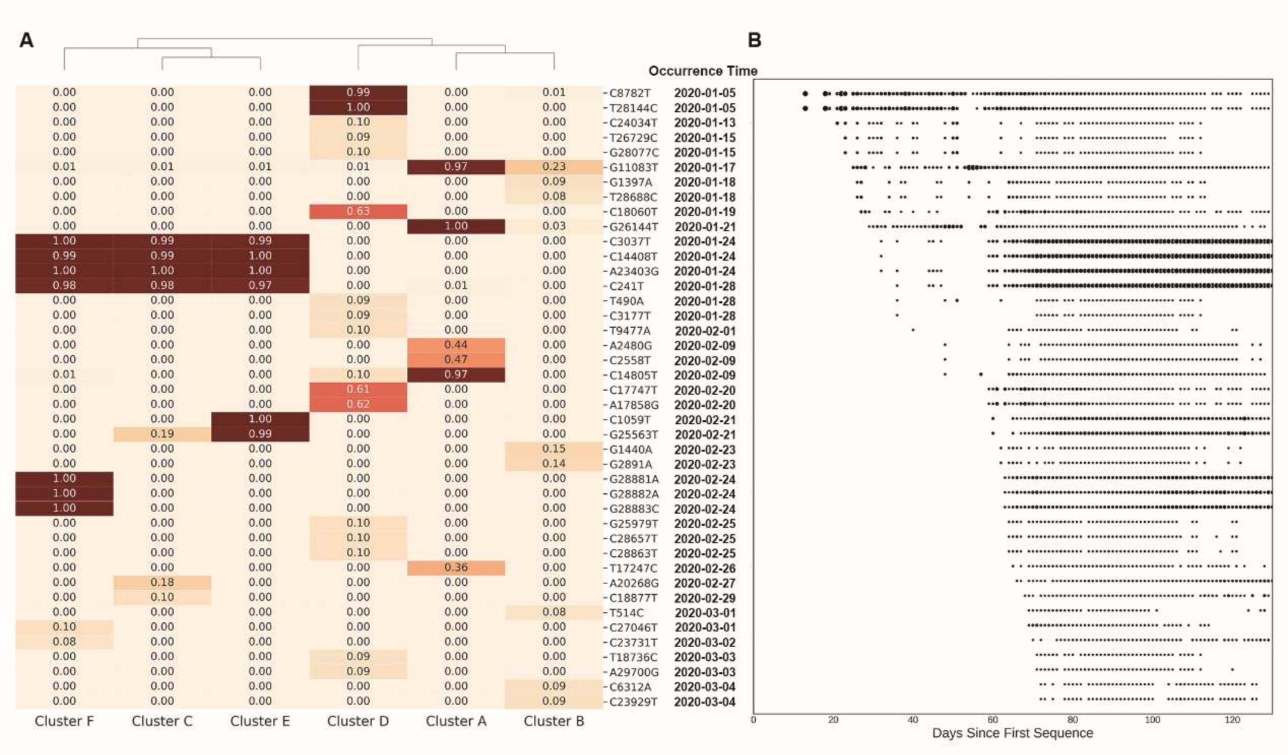

Cluster F	Cluster C	Cluster E	Cluster D	Cluster A	Cluster B		Occurrence Time
0.00	0.00	0.00	0.99	0.00	0.01	C8782T	2020-01-05
0.00	0.00	0.00	1.00	0.00	0.00	T28144C	2020-01-05
0.00	0.00	0.00	0.10	0.00	0.00	C24034T	2020-01-13
0.00	0.00	0.00	0.09	0.00	0.00	T26729C	2020-01-15
0.00	0.00	0.00	0.10	0.00	0.00	G28077C	2020-01-15
0.01	0.01	0.01	0.01	0.97	0.23	G11083T	2020-01-17
0.00	0.00	0.00	0.00	0.00	0.09	G1397A	2020-01-18
0.00	0.00	0.00	0.00	0.00	0.08	T28688C	2020-01-18
0.00	0.00	0.00	0.63	0.00	0.00	C18060T	2020-01-19
0.00	0.00	0.00	0.00	1.00	0.03	G26144T	2020-01-21
1.00	0.99	0.99	0.00	0.00	0.00	C3037T	2020-01-24
0.99	0.99	1.00	0.00	0.00	0.00	C14408T	2020-01-24
1.00	1.00	1.00	0.00	0.00	0.00	A23403G	2020-01-24
0.98	0.98	0.97	0.00	0.01	0.00	C241T	2020-01-28
0.00	0.00	0.00	0.09	0.00	0.00	T490A	2020-01-28
0.00	0.00	0.00	0.09	0.00	0.00	C3177T	2020-01-28
0.00	0.00	0.00	0.10	0.00	0.00	T9477A	2020-02-01
0.00	0.00	0.00	0.00	0.44	0.00	A2480G	2020-02-09
0.00	0.00	0.00	0.00	0.47	0.00	C2558T	2020-02-09
0.01	0.00	0.00	0.10	0.97	0.00	C14805T	2020-02-09
0.00	0.00	0.00	0.61	0.00	0.00	C17747T	2020-02-20
0.00	0.00	0.00	0.62	0.00	0.00	A17858G	2020-02-20
0.00	0.00	1.00	0.00	0.00	0.00	C1059T	2020-02-21
0.00	0.19	0.99	0.00	0.00	0.00	G25563T	2020-02-21
0.00	0.00	0.00	0.00	0.00	0.15	G1440A	2020-02-23
0.00	0.00	0.00	0.00	0.00	0.14	G2891A	2020-02-23
1.00	0.00	0.00	0.00	0.00	0.00	G28881A	2020-02-24
1.00	0.00	0.00	0.00	0.00	0.00	G28882A	2020-02-24
1.00	0.00	0.00	0.00	0.00	0.00	G28883C	2020-02-24
0.00	0.00	0.00	0.10	0.00	0.00	G25979T	2020-02-25
0.00	0.00	0.00	0.10	0.00	0.00	C28657T	2020-02-25
0.00	0.00	0.00	0.10	0.00	0.00	C28863T	2020-02-25
0.00	0.00	0.00	0.00	0.36	0.00	T17247C	2020-02-26
0.00	0.18	0.00	0.00	0.00	0.00	A20268G	2020-02-27
0.00	0.10	0.00	0.00	0.00	0.00	C18877T	2020-02-29
0.00	0.00	0.00	0.00	0.00	0.08	T514C	2020-03-01
0.10	0.00	0.00	0.00	0.00	0.00	C27046T	2020-03-01
0.08	0.00	0.00	0.00	0.00	0.00	C23731T	2020-03-02
0.00	0.00	0.00	0.09	0.00	0.00	T18736C	2020-03-03
0.00	0.00	0.00	0.09	0.00	0.00	A29700G	2020-03-03
0.00	0.00	0.00	0.00	0.00	0.09	C6312A	2020-03-04
0.00	0.00	0.00	0.00	0.00	0.09	C23929T	2020-03-04

Figure 4. The clustering of the six clusters by the extracted mutations. (**A**) The heatmap displays mutation frequency of the 42 mutations across six clusters. The colors and values represent different frequencies of the corresponding mutations in each cluster. The collected days of the mutations are represented in (**B**). The X axis represents the days from the corresponding collection date of strains to 24 December 2019 when the earliest strain (EPI_ISL_402123) was collected. Circle sizes represent the frequency the of the mutations on each collection day.

Supplementary Information

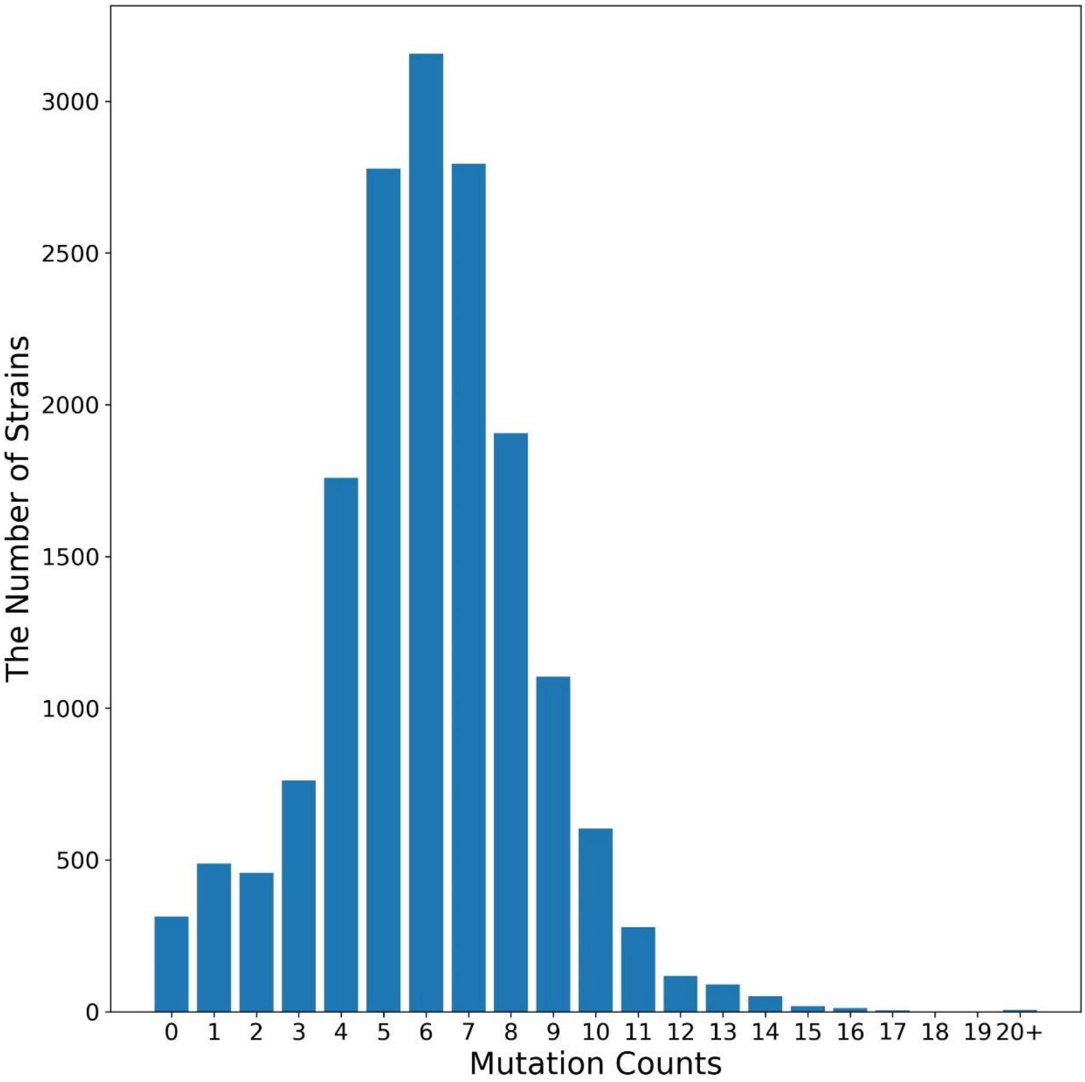

Figure S1. The distribution of the mutation counts of the 16,873 SARS-CoV-2 strains.

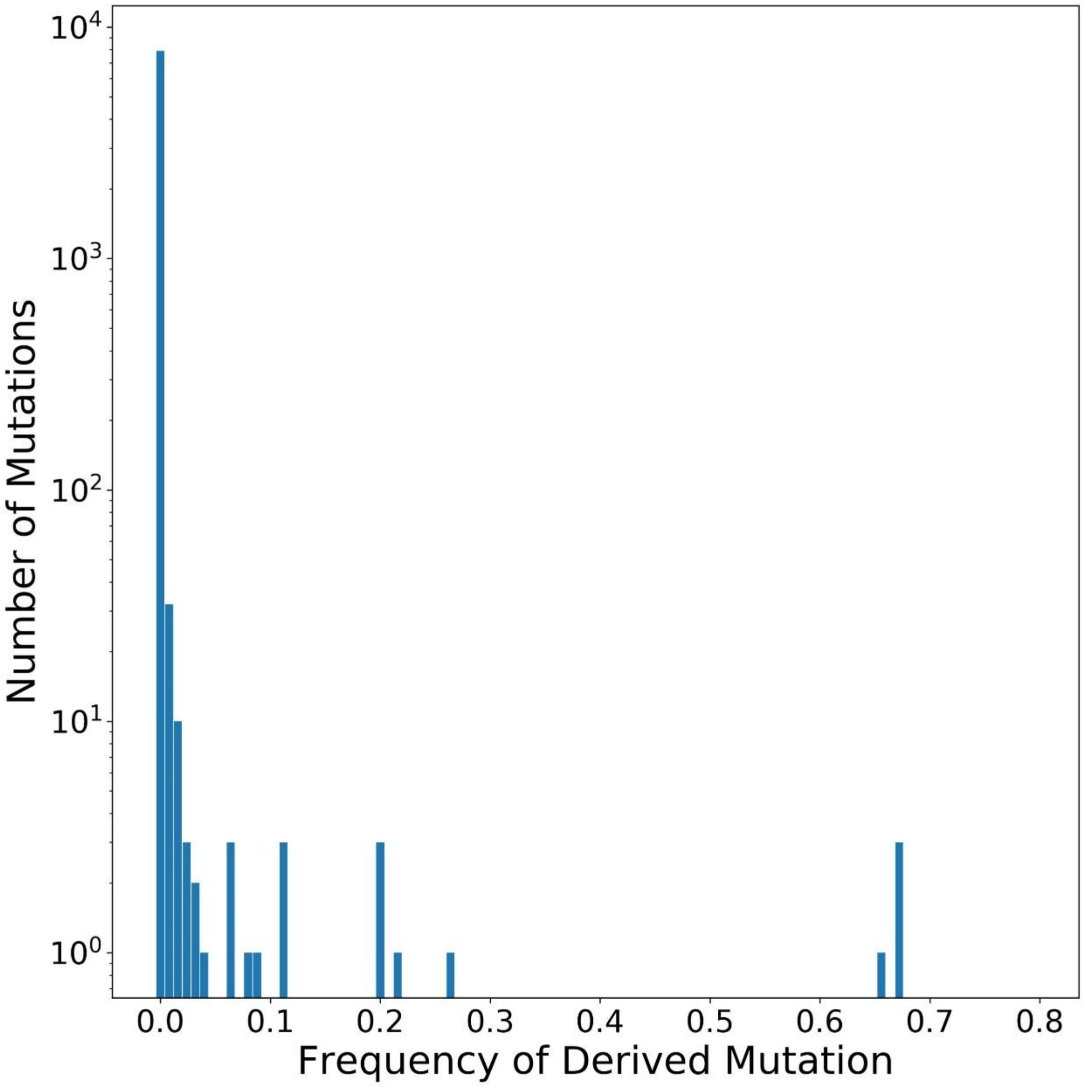

Figure S2. Frequency spectra of SARS-CoV-2. The mutation frequency of derived mutations of 16,873 SARS-CoV-2 stains is depicted on the X axis, and the number of mutations in which strains occurred is displayed on the Y axis. A log-10 scale is used for the Y axis of the graph, and the Y axis ranges from 1 to 10,000.

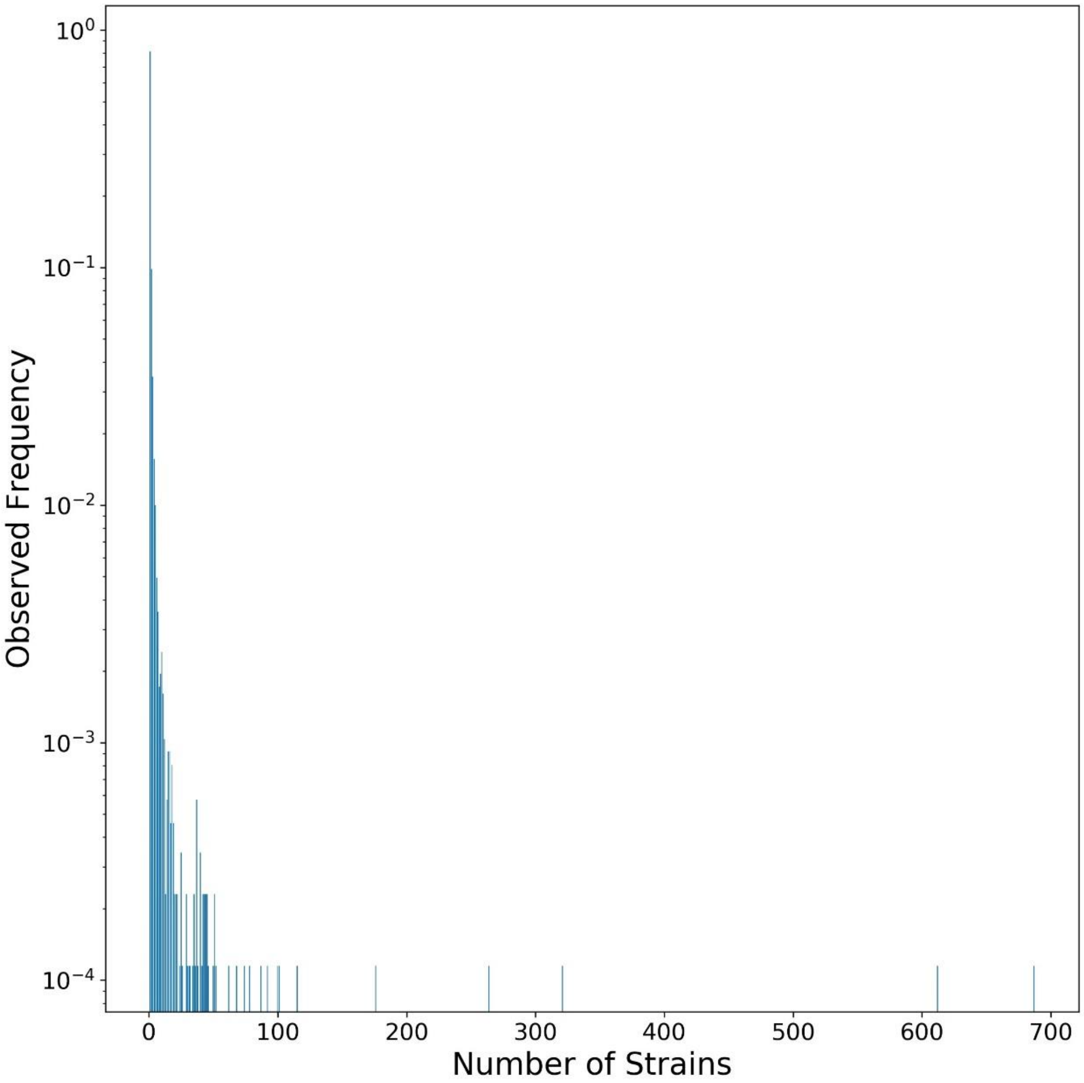

459

460

461 **Figure S3.** Normalized allele frequency of 16,873 SARS-CoV-2 strains. There are 8,706 unique genomes across the 16,873

462 strains. The X axis is the number of strains for each unique genome and the Y axis is the proportion of the unique genomes.

463 A log-10 scale is used for the Y axis of the graph, and the Y axis ranges from 0.0001 to 1.

464

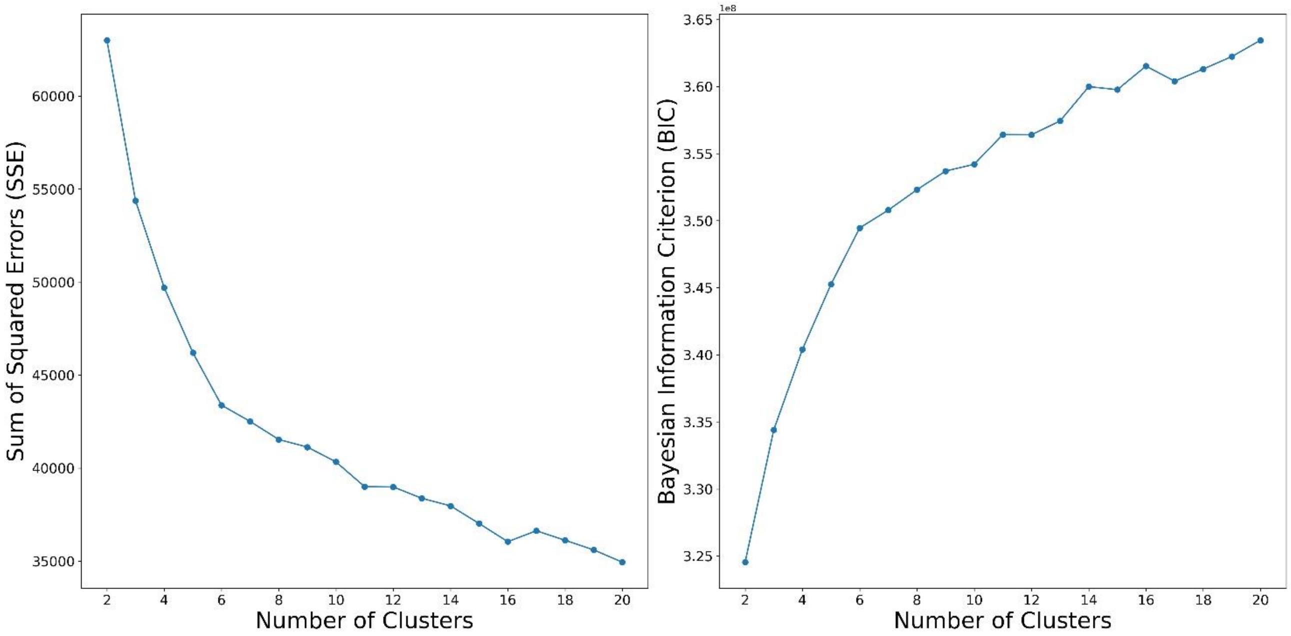

Figure S4. Evaluation of the number of clusters. The evolution of the sum of squared errors (SSE; left) and Bayesian information criterion (BIC; right) for the number of clusters in the deep learning clustering runs. We used the elbow method and chose the elbow of the curve as the number of clusters. The elbow method indicated that the number of clusters is six.

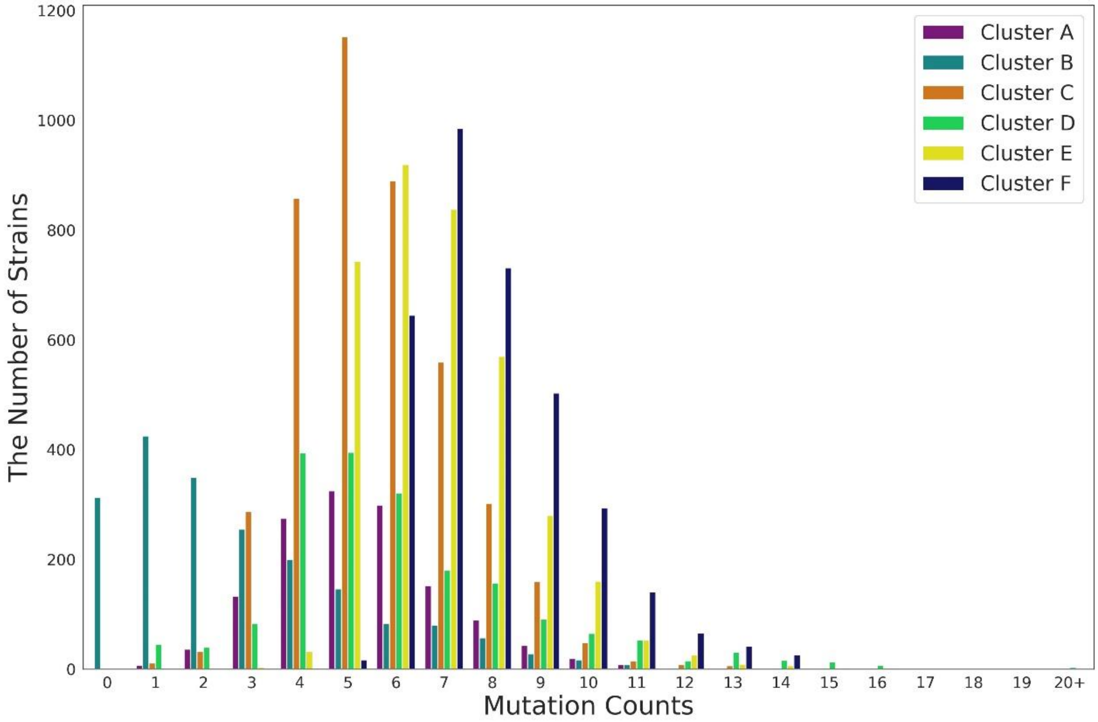

Figure S5. The distribution of the mutation counts of the strains for the six clusters.

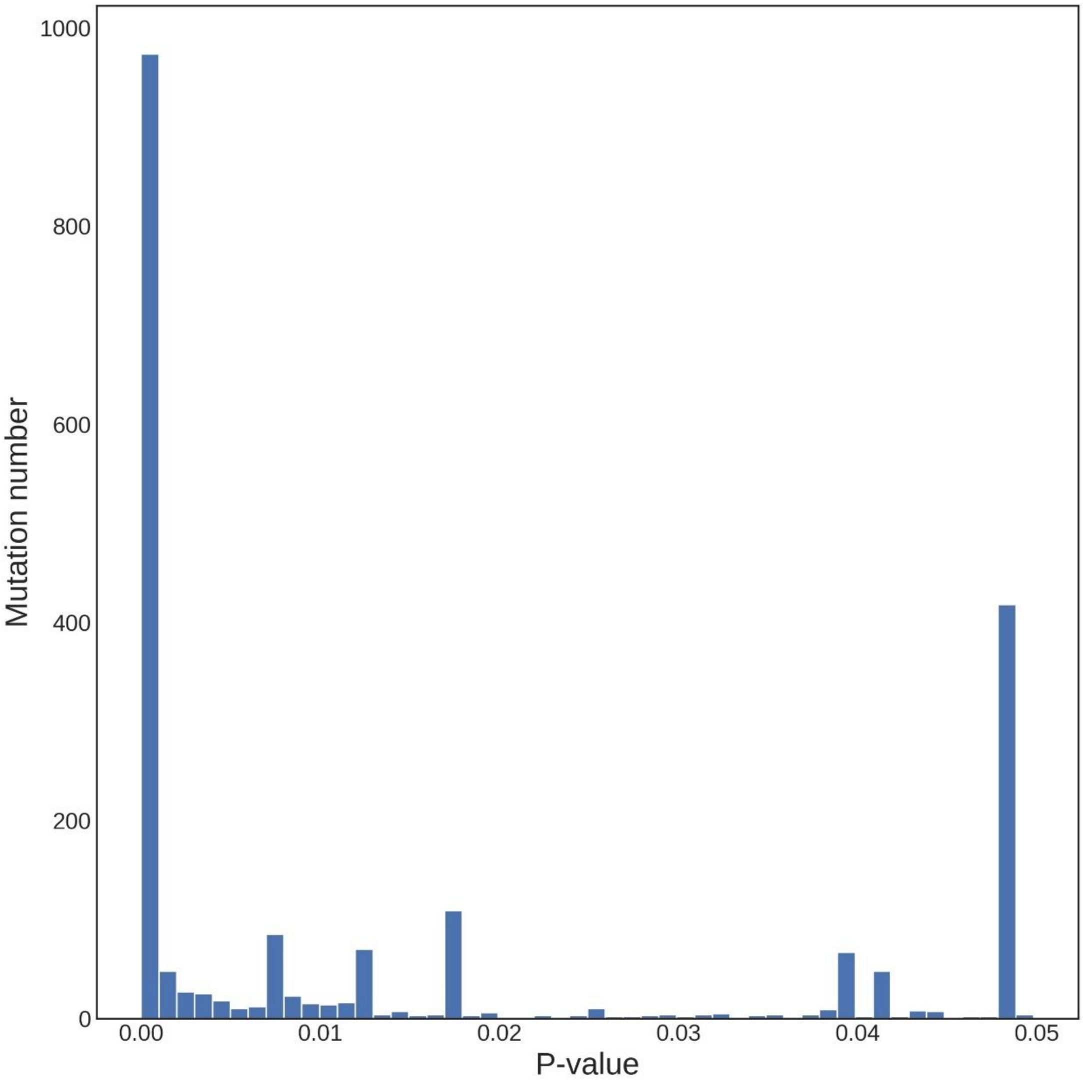

Figure S6. The distribution of P-values from the 2,094 mutations with P-values <0.05 by ANOVA.

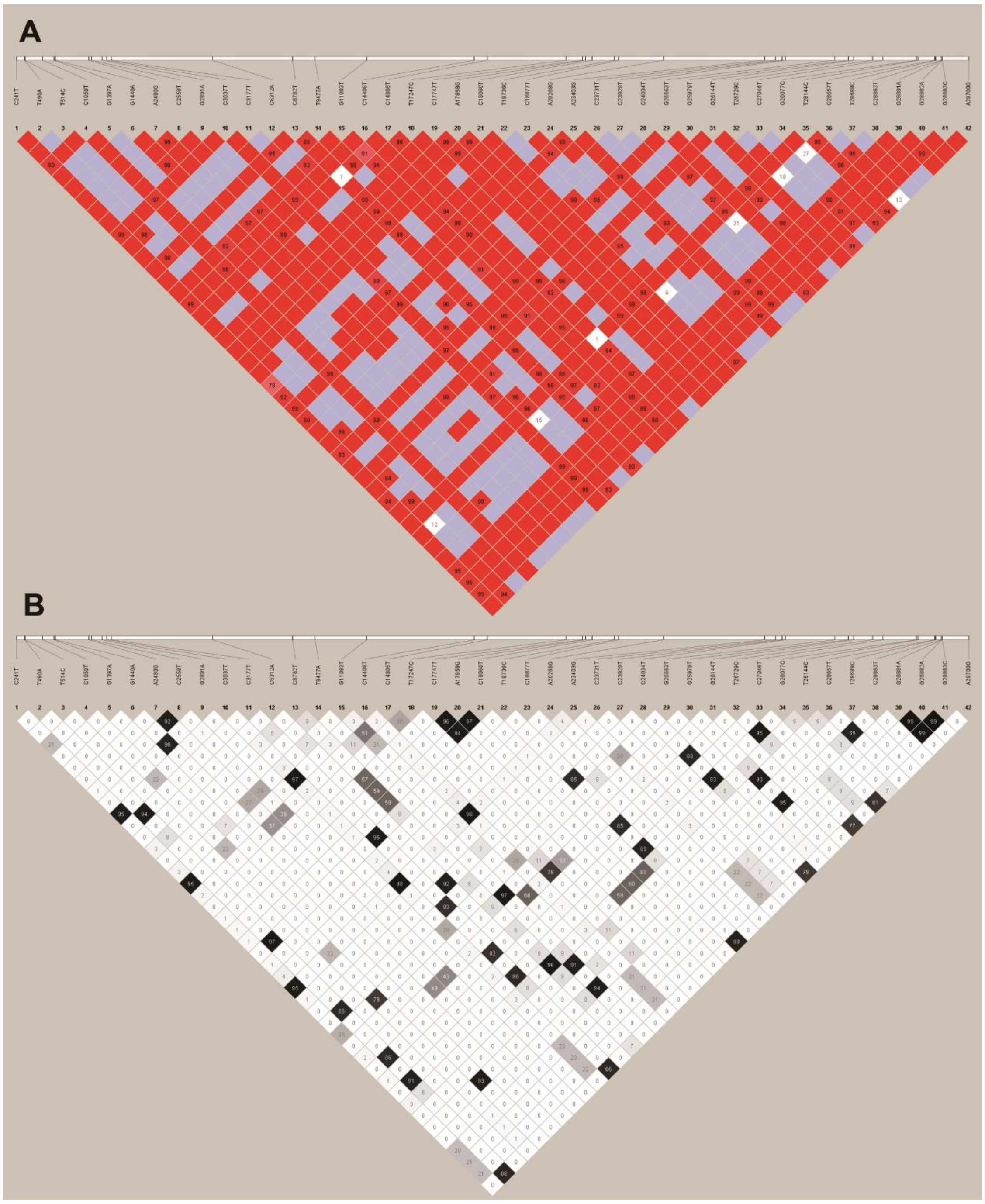

Figure S7. The D’ and r^2 of the 42 mutations. (**A**) D’ values that correspond to substitution pairs are expressed as percentages and are shown within the respective squares. Higher D’ values are indicated with a brighter red color. (**B**) The numbers within the squares represent the r^2 scores for pairwise LD. r^2 values are represented by white for $r^2 = 0$, with intermediate values for $0 < r^2 < 1$ indicated by shades of grey.

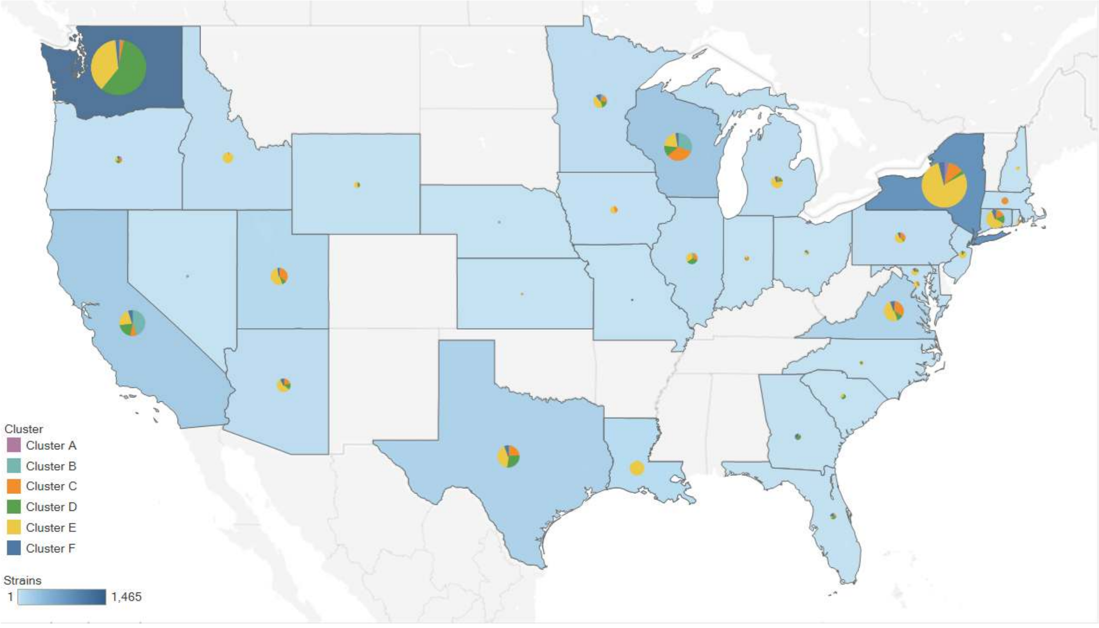

Figure S8. Geographic distribution of six clusters in the United States. Pie charts display the proportions of six clusters among all SARS-CoV-2 strains in each state. Circle sizes and the color scales correspond to the number of strains analyzed per state.

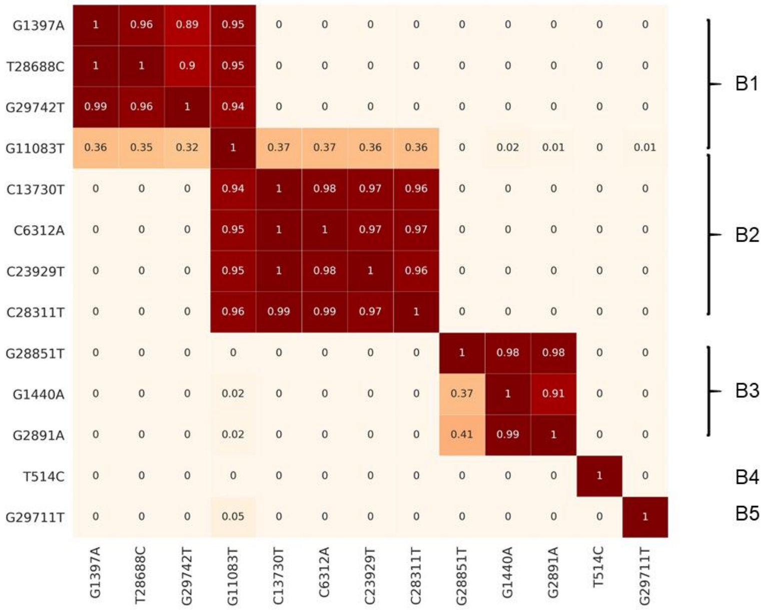

Figure S9. The pairwise dependency score (see Materials and Methods) of the mutations with frequency >0.05 within cluster B. The heatmap shows that there are five major subclusters within cluster B.

Table S1 Geographic distribution of six continents for each cluster.

Cluster	Cluster A	Cluster B	Cluster C	Cluster D	Cluster E	Cluster F	Total
Africa	3	4	65	7	10	9	98
Asia	38	648	248	217	57	116	1,324
Europe	1,137	990	3,119	212	1,108	2,961	9,527
North America	94	334	625	1,268	2,274	170	4,765
Oceania	110	161	233	196	191	149	1,040
South America	6	5	44	10	5	49	119
Total	1,388	2,142	4,334	1,910	3,645	3,454	16,873